Measurement 225 (2024) 113870

Contents lists available at ScienceDirect

Measurement

journal homepage: www.elsevier.com/locate/measurement

Infrared temperature measurements on fast moving targets: A novel calibration approach

Manuela Sisti [a,*], Chiara Falsetti [b], Paul F. Beard [a]

[a] University of Oxford, Department of Engineering Science, Thermofluids Institute, Oxford, United Kingdom
[b] Delft University of Technology, Faculty of Aerospace Engineering, Propulsion and Power, Delft, Netherlands

ARTICLE INFO

Keywords:
Infrared thermography
High-speed target
Turbomachinery
Measurement advancements

ABSTRACT

In this study, an infrared system is developed for accurate measurements of surface temperature and heat transfer on fast moving targets. The system was designed for the Oxford Turbine Research Facility, a world-leading experimental facility delivering highly engine representative, scalable heat transfer results for aerospace research. Infrared thermography is employed to acquire temperature maps of high-pressure turbine blades, allowing assessment of surface thermal conditions including heat transfer coefficient, adiabatic wall temperature, Nusselt number, cooling effectiveness, and metal effectiveness.

Achieving accurate infrared thermography measurements in rotating turbomachinery experimental conditions is arduous due to reflections from the surroundings, low emissivity of metallic parts, and motion blur resulting from high speed. To overcome these challenges, calibration procedures were developed against a traceable standard using a bespoke steady experimental facility. A method to determine the reflected temperature from surroundings was also validated. Correction for all measurement disturbances is demonstrated to within the accuracy of the primary measurement thermocouple.

Finally, the developed calibration method was validated on a fast-moving rotating geometry demonstrating accurate correction for all measurement disturbances, without the need for an in situ calibration. A detailed uncertainty analysis for each calibration step is also presented.

1. Introduction

Efforts to enhance efficiency and reduce emissions in gas turbines have resulted in increased turbine entry temperatures, requiring the adoption of more efficient cooling methods to ensure component durability. Highly engine-representative aerothermal experiments are necessary for understanding thermal behaviours and developing effective cooling systems. Additionally, accurate experimental data is needed to enhance the reliability of simulations employed in the engine design phase.

Traditionally, temperature has been measured by thermocouples and resistance temperature detectors (RTDs). However, these instruments give information on a single point and can also impact the aerodynamics, e.g. tripping the boundary layer. In situations where a high spatial and temporal temperature variation is expected, these techniques can be limiting. In comparison, infrared (IR) thermography is fully two-dimensional, non-intrusive, and modern detectors can provide analysis on high-speed moving targets. As such, it is a highly valuable tool for turbine heat transfer research.

Historically, IR thermography has been widely used in wind tunnels and non-rotating cascade facility for aerospace research, becoming a standard tool for the aerothermal study of several applications: film cooling testing, aerofoils and endwalls heat transfer testing in linear cascades, and blade tip heat transfer. A thorough review of IR thermography used in convective heat transfer studies can be found in [1].

An extensive review of calibration studies for both pyrometer and IR cameras in turbomachinery applications is presented by Falsetti et al. [2]. The common approach, especially for stationary targets, is to calibrate the infrared thermography system in situ employing thermocouples embedded in the object surface. A calibration curve can then be obtained to correlate the camera raw signal to the real target temperature, simultaneously accounting for surroundings reflections and emissivity effects. This is the approach behind the in situ method proposed by Martiny et al. [3] and proven by Schulz [4] for film cooling in gas turbine components. Further development of this method to allow for better accuracy of extrapolated temperatures necessary whenever thermocouples do not cover the whole temperature span present across the specimen at all operating points, were presented by Ochs et al. [5]. The authors reduced the fitting parameters of the

* Corresponding author.
E-mail addresses: manuela.sisti@eng.ox.ac.uk (M. Sisti), C.falsetti@tudelft.nl (C. Falsetti), paul.beard@eng.ox.ac.uk (P.F. Beard).

https://doi.org/10.1016/j.measurement.2023.113870
Received 16 May 2023; Received in revised form 27 August 2023; Accepted 13 November 2023
Available online 10 December 2023

in situ calibration by performing a pre-calibration at steady ambient temperature where the experimental set-up is replicated. The purpose of the in situ calibration was to account for the impact of the higher mainstream temperature on the offset signal. The authors were able to reduce the maximum errors from 12% [3] to 1.2% of the temperature range.

The studies discussed so far assume a homogeneous surroundings temperature distribution and a constant surface emissivity. These assumptions can fail in particular situations, such as highly spatial dependent surroundings temperature distribution and angle of view larger than 50-deg. Elfner et al. [6], drawing on Ochs et al. [5], performed a geometrical ray-tracing analysis to compute a correction factor for reflections that varied spatially. In the same scope, Kirollos and Povey [7] proposed the use of a Reflective Marker Array (RMA) to obtain spatial data of reflected temperature. By spatially resolving the reflection distribution, Elfner et al. [6] demonstrated that the error could be reduced from 8% to 2% at a surface temperature of 350 K, while Kirollos and Povey [7] proved the capability of their method of reducing the maximum error from 6 °C (using a single value for the reflected temperature), to 1.5 °C at a temperature range of 38 °C–56 °C. The RMA method [7] was also applied by Jonsson et al. [8] to experimentally investigate the heat transfer coefficient of a heated outlet guide vane, obtaining results to within an uncertainty of 2.5% – 8% of reading.

These calibration methods were developed for stationary targets, and all require reference temperature sensors installed onto the target. However, when calibrating an IR thermography system for fast moving rotating targets, complications arise due to the practicality of thermocouple installation and telemetry of data off-shaft. Therefore, such methods have their limitations. In addition, the effect of motion blur needs to be addressed. This is especially fundamental when detecting the temperature gradients of small features, such as in the vicinity of cooling holes on a blade surface.

There are few published studies focused on IR thermography temperature measurements on fast moving, rotating surfaces. This was mainly due to limitations in the acquisition speed of the detector, in other words, limitation in the maximum frame rate and minimum achievable integration time. The maximum frame rate limits the number of images captured during each revolution, while the minimum integration time will affect the image quality in terms of blur. With the advent of IR cameras capable of working with very low integration times (order of μs), first attempts to use IR thermography on rotor blades were published. Mori et al. [9] carried out a study on the pressure side of a rotor blade with a rotational speed up to 1500 rpm working with an integration time of 100 μs. Nevertheless, the application of IR thermography to high-speed rotating rigs, such as highly engine representative turbine rigs spinning on order of 10,000 rpm, is still very rare. If not properly characterised and reconstructed, the speeds involved are such that the effect of motion blur can make the use of IR thermography very challenging, only three research groups have published studies on this topic. In chronological order, these are: Lazzi Gazzini et al. [10] at the ETH Zurich, Christensen et al. [11] at the Ohio State University, and Knisely et al. [12] at the PennState University.

Lazzi Gazzini et al. [10] exploited IR thermography to study heated rotor endwalls of the turbine in the long duration LISA facility, with rotor speed of 2700 rpm using a FLIR SC7300L camera. The authors addressed the problem of motion blur by merging two pairs of images captured at consistent conditions but with different integration times, 10 μs and 50 μs. The short integration time produces a sharper image but with higher noise level, while the longer integration time supplies a more accurate temperature level but with a higher motion blur. A blind deblurring algorithm is applied to the long exposure images, followed by a frequency study of both images to identify deblurring artifacts. Finally, high and low pass filters are used to eliminate white noise and ringing.

Christensen et al. [11] used IR thermography to assess the temperature of a cooled rotor blade tip rotating at 13,000 rpm with tip speed of approximately 300 m s^{-1} using a FLIR X6901sc SLS camera. The Ohio State University Turbine Test Facility operates with a run time of 120 ms, which limits the surface temperatures to 350 K. Given the high speed and relatively low target temperature, the authors faced similar motion blur challenges. The authors selected an integration time of 47.6 μs as compromise between signal intensity and motion blur. A deblurring non-blind Wiener filter is applied to the raw infrared images. This filter required knowledge of the expected motion blur, which was predicted using 3-D models and particle image velocimetry software.

Finally, Knisely et al. [12] outlined a procedure to assess an infrared detector for high-speed rotating tests providing recommendations for accurate IR measurements. The goal was to use the IR imaging system in the Steady Aero Research Turbine Laboratory on blades rotating at 10,000 rpm. The authors stated that a short integration time (1–2 μs) can be selected despite low target temperature level, if a minimum of 100 images are averaged. In a following study [13], a 2 μs integration time and averaged 200 images was adopted to assess the overall effectiveness and life or turbine blades. Clearly, this was achievable thanks to the continuous duration mode of the facility. The authors did not develop any deblurring technique, but contrarily lowered the integration time to a minimum. The literature review evidences that there is still considerable work to do to thoroughly understand the applicability of IR thermography to fast moving targets, and particularly in accurately quantifying and minimising the error.

The present study aims at filling this gap by conceiving accurate and novel calibration and processing methods. The overarching objective of this work is to develop an IR thermography measurement system for the Oxford Turbine Research Facility (OTRF). The work concentrates on measurements of the rotor temperature, with targets spinning up to 10,000 rpm, which translates to approximately 250 m s^{-1} tangential tip speed.

The results presented in this paper enhance the understanding of IR measurement techniques, whilst providing useful guidance for developing an IR measurement system for high-speed targets. The calibration method detailed in this study does not require a reference temperature sensor to be installed on the target (e.g. a turbine blade), therefore reducing the technical difficulty. The semi in situ calibration is conducted in two experimental facilities: (i) a steady calibration facility, and (ii) a rotating facility with limited optical access, such as in turbomachinery. The former is used to calibrate the camera detector, assess the target directional emissivity, determine the optical window transmittance, and as a proof of concept for the reflections correction method. The latter is used to test the reflections correction method on a rotating system and to illustrate the effect of motion blur on the calibration.

1.1. Infrared thermography in the OTRF

The OTRF, shown in Fig. 1(a), is a transient rotating facility with a run time of approximately 500 ms, and the capability of testing high pressure turbine stages under conditions that are representative of actual engine operation. The facility can match Mach and Reynolds numbers, non-dimensional speed and gas-to-wall temperature ratio. Recent research studies conducted in the OTRF have been reviewed by Chana et al. [14] and Falsetti et al. [15].

An upgrade is currently being developed, this will allow a semi-transient test mode by prolonging the run time to 60 s, and enable testing at gas-to-wall temperature ratios representative of modern civil aerospace engines, increasing from 1.5 to 2. The implementation of the infrared thermography system discussed in this paper will also be made possible by this upgrade, enabling comprehensive surface heat transfer measurement on all rotor blade surfaces.

This study uses a FLIR A6751 SLS LWIR camera, which was chosen for its sensitivity and speed. The camera features a 640 × 512

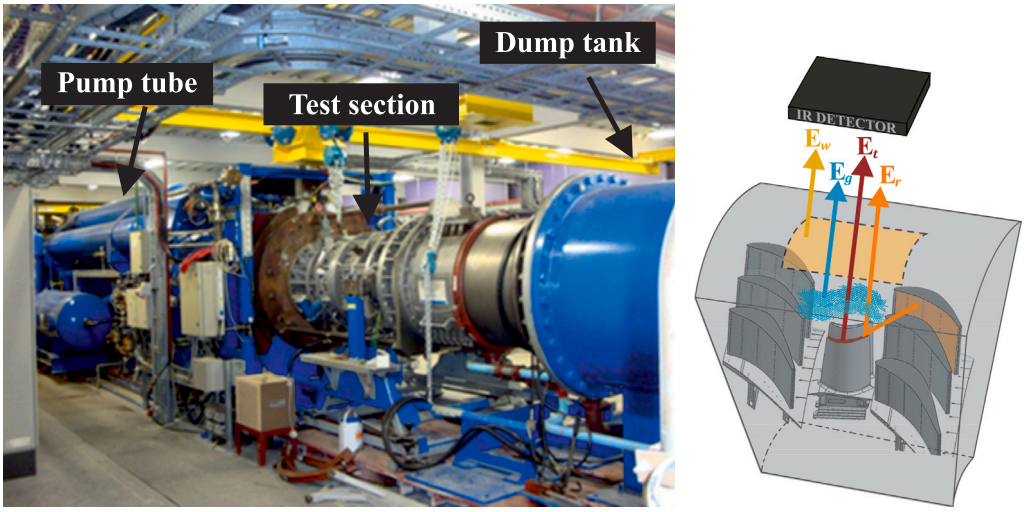

Fig. 1. (a) Image of the OTRF test section; (b) Schematic highlighting the energy components detected by an infrared system in a turbomachinery experiment [2], where E_t is the energy from the target, E_r the energy from surroundings reflected on the target, E_w the energy from the IR-transparent window, and E_g the energy from the mainstream gas.

pixel Focal Plane Array (FPA) and cooled Strained Layer Superlattice (SLS) detector, sensitive to the wavelength in the long infrared range, between 7.5 μm and 10.5 μm, which suits the expected experimental peak emission of 9 μm approximately. The camera has a minimum integration time of 0.480 μs, and a frame rate of 125 Hz. The option to increase the frame rate is available by windowing down at the Focal Plane Array (FPA) level.

The various contributions of the total radiation energy reaching an IR camera imaging a typical turbine geometry are depicted in Fig. 1(b). Within this schematic representation, the focus of the measurement is marked in red and centres on the rotor blade tip. The nearby surroundings include the stator vanes; as an illustrative example, one vane is highlighted in orange. The optical path consists of the mainstream gas and the IR transparent window. The mainstream gas is shown in blue and consists of dry air in the OTRF. The IR transparent window is highlighted in a yellow hue. In the OTRF, the window is made of Zinc Selenide and has a thickness of approximately 1.7 cm. In addition to the radiation emitted by the target of interest (E_t), the detector also receives offsetting radiation. This disturbance signal comprises two components: (i) the radiation emitted from the surroundings that reflects off the target surface, and undergoes attenuation as it travels along the optical path, and (ii) the radiation emitted by the optical path, mainstream gases and IR-transparent window.

Using the *Stefan–Boltzmann* equation, the total energy detected can be expressed in terms of temperature as:

$$T_{cam}^4 = \tau_{opt}\varepsilon_t T_t^4 + \tau_{opt}(1-\varepsilon_t)T_r^4 + (1-\tau_{opt})T_{opt}^4 \tag{1}$$

and rearranged as:

$$T_t^4 = \frac{T_{cam}^4}{\tau_{opt}\varepsilon_t} - \frac{(1-\varepsilon_t)T_r^4}{\varepsilon_t} - \frac{(1-\tau_{opt})T_{opt}^4}{\tau_{opt}\varepsilon_t} \tag{2}$$

The measured equivalent blackbody temperature, T_{cam}, is affected by the surroundings reflected temperature, T_r, and the optical path temperature, T_{opt}. Therefore, accurate measurement of the target temperature, T_t, requires knowledge of the above as well as of the emissivity, ε_t, the transmittance, τ_{opt}, and the calibration procedures to quantify these terms need to be optimised.

The relative contribution of the target and disturbance signals is strongly dependent on the surface emissivity. The varying contributions to the signal for a typical experiment in the OTRF are presented in Fig. 2. The analysis was conducted for emissivity values varying from $\varepsilon = 0.04$, typical of polished metals, to $\varepsilon = 0.94$, obtained from the calibration of a high emissivity coating described in the next section. Results for an intermediate value of $\varepsilon = 0.6$ are also shown. Increasing the emissivity of the target greatly reduces the contribution of the disturbance signal, including reflections and optical transmittance, which reduces from approximately 97% with $\varepsilon = 0.04$ to 10% with $\varepsilon = 0.94$. Indeed, applying high emissivity paint on the target surface is a widely adopted practice, especially when the material has low emissivity, such as polished metals.

Table 1
Sensitivity analysis on the target temperature, T_t, of assumed value 500 K.

Variable		Expected values	C_i
Equivalent blackbody temperature	T_{cam}	500.5 K	1.122
Target emissivity	ε_t	0.94	0.115
Optical path transmittance	τ_{opt}	0.95	0.127
Surroundings reflected temperature	T_r	550 K	0.095
Optical path temperature	T_{opt}	430 K	0.031

Table 1 presents the outcomes of a sensitivity analysis performed on Eq. (2), also using expected temperature values of T_t, T_r, T_{opt} for a typical OTRF test. Values of ε_t, and τ_{opt} were taken from calibration data presented later. The sensitivity coefficients, $C_i = (T_t - T_{t,+1\%})/(T_t) \cdot 100$, express the change in the evaluated target temperature when the corresponding parameter is varied by 1%. The temperature detected by the camera, T_{cam}, presents the highest sensitivity coefficient with 1% error translating into 1.12% net error on T_t. It can be inferred that to ensure an accurate measurement, particular attention must be given to the error in the evaluation of T_{cam}; thus to the calibration from digital counts to blackbody equivalent temperature, discussed in Section 2.1. The sensitivity coefficient for the equivalent blackbody temperature is followed by the sensitivity coefficients for emissivity and transmittance, that have approximately the same magnitude. Finally, reflected temperature and optical path temperature present the lowest sensitivity coefficients.

Results from this analysis are to be considered valid for the specific temperatures and radiative conditions presented. The performance is highly interconnected and changing one variable strongly affects the results. Fig. 3 shows the variation of sensitivity coefficients as a function of target emissivity, calculated with the same expected values for temperatures and transmittance as above. At lower emissivity values, the variable that dominates the error in target temperature becomes the reflected temperature, T_r.

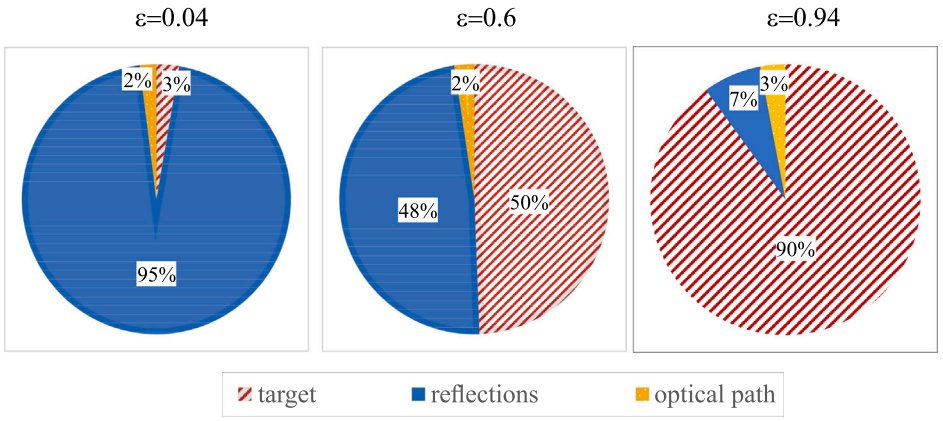

Fig. 2. Contributions of target, surroundings and optics radiances to the total detected radiance (Eq. (1)) for nominal expected values of T_i = 500 K, T_r = 550 K, T_{opt} = 430 K $\tau = 0.95$ and for three emissivity value $\varepsilon = 0.04$, $\varepsilon = 0.6$ and $\varepsilon = 0.94$.

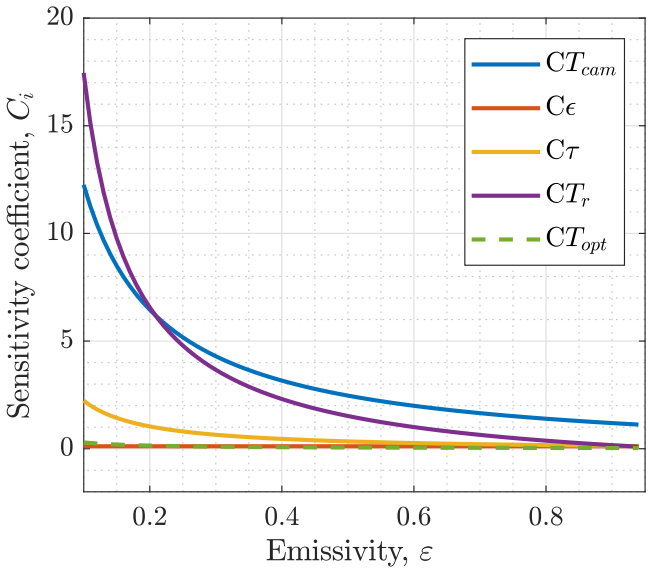

Fig. 3. Impact of emissivity on influence coefficients C_i.

As Figs. 2–3 outline, increasing the target emissivity is a fundamental step in order to reduce the error. Nevertheless, the calibration procedures for the different sources of error need to be optimised according to the specific testing environment to obtain the best possible accuracy.

2. Steady system calibration

A bespoke steady-state facility was developed to perform traceable calibration of the detector, surface emissivity and optical path transmittance. This facility was also used to prove the concept of a novel method to correct for disturbance signal caused by reflecting radiation. The photograph in Fig. 4a shows the set-up for the detector calibration, where a blackbody source is placed in front of the camera at a distance of 250 mm. The enclosure, made of black Foamex PVC with a matt finish, serves to shield the calibrator and camera from extraneous radiation. The set-up used for the emissivity measurements as a function of temperature and viewing angle is shown in Fig. 4b, where a bespoke emissivity calibrator is placed in front of the camera. A sectional view of the emissivity calibrator is shown in Fig. 4c. An assembly is created by positioning a thin copper plate measuring 150 × 100 mm and having a thickness of 5 mm between two layers of ROHACELL®. These layers have overall dimensions of 230 × 180 mm and feature varying thicknesses, 40 mm at the back side and 20 mm at the front side. ROHACELL® is known for its thermal conductivity, approximately 0.03 W m^{-1} K^{-1}. To further boost thermal stability, the entire assembly is encased in Perspex®. An electrical silicone heating element, powered by a variable power supply, is mounted behind the sample. Eight T-type thermocouples are surface mounted on the front and back of the copper sample to measure the temperature uniformity and serve as reference for the calibration. The signal from the thermocouples was monitored during the heating phase, and data from the thermocouples and IR camera were acquired simultaneously when steady state condition was reached, defined as a thermocouple signal standard deviation <0.02 K. The emissivity of different coatings was evaluated, including black matt paint and aluminium tape. To allow measurements of directional surface emissivity, the calibrator was mounted on a rotary stage. The transmittance of a sample of ZnSe window was also determined. The window was interposed between the blackbody source and the camera replicating the relative position of the camera, window and target relative position expected in the actual experiments.

In the following sections, the detector, surface emissivity and transmittance calibrations are described in detail.

2.1. Detector calibration

To obtain a temperature map from the raw digital counts signal acquired by an IR camera, a detector calibration is required. A blackbody source was used to irradiate the Focal Plane Array (FPA) at a range of temperatures, $T_{bb,i}$. Data were averaged over 100 frames acquired at 125 Hz. Two blackbody sources, the CI-Systems SR33-7 and the Fluke 4181, were used. Both calibrators are NIST traceable. The combined uncertainty of the calibrator which was calculated by taking the root sum square of the accuracy, uniformity, and stability errors [17,18], was used to determine the temperature range for each source, the CI-Systems calibrator was used in the range 293.15 K–353.15 K, and the Fluke 4181 in the range 353.15 K–543.15 K. The two uncertainties as a function of temperature are compared in Fig. 5.

The approache detailed by Schulz et al. [19] was used to correct for the photoresponse non-uniformity arising in a FPA due to inherent differences in each individual detector element. A linear correction was applied pixel-wise by finding two parameters via curve fitting, the gain, m_{xy}, and the offset, q_{xy}. These identify the relationship between the deviation from the mean, $\Delta R_{x,y}$, and the mean over the entire FPA $\langle R \rangle$ as follows:

$$\Delta R_{i,xy} = m_{xy}\langle R_i \rangle + q_{xy} \tag{3}$$

The digital count signal is corrected as follows:

$$R^c_{i,xy} = \frac{R_{i,xy} - q_{xy}}{1 + m_{xy}} \tag{4}$$

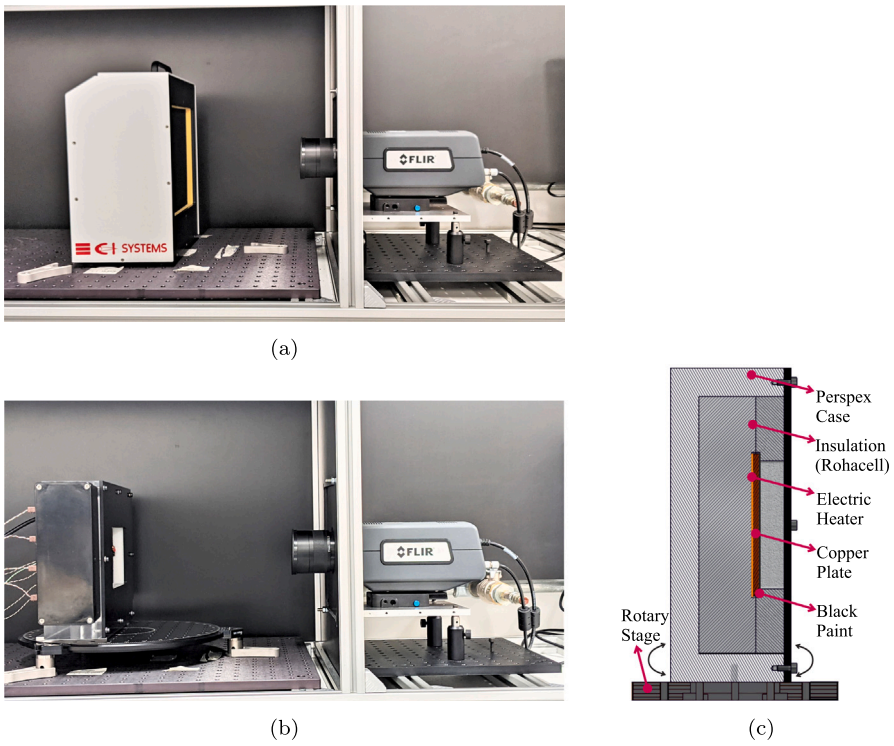

Fig. 4. Steady calibration facility set-ups for (a) detector calibration, and (b–c) emissivity calibration [16].

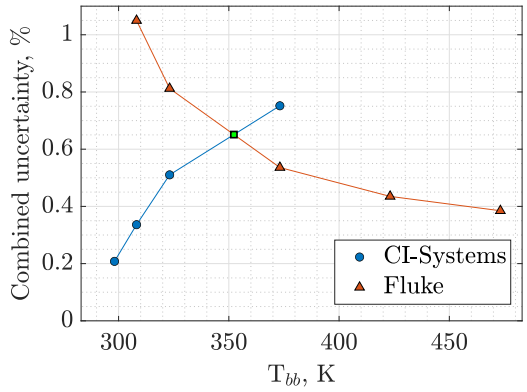

Fig. 5. Stability, uniformity and accuracy combined uncertainty for the two blackbody sources used in the study.

Subsequently, the corrected pixel digital count ($R^c_{i,xy}$) is used for the radiometric pixel-by-pixel blackbody calibration, which relates the detector signal to the temperature of the blackbody source (T_{bb}) using a fourth order polynomial fitting.

The detector calibration and saturation are inherently a function of temperature and integration time. To capture high quality images of rotating objects a low integration time is needed. The required integration time will be dependent of target speed and acceptable blur level. For instance, for a rotor speed of 4000 rpm, with a radius of 0.260 m, an integration time of 50 µs gives an estimated blur in the direction of motion of $v_t \cdot \mathrm{IT} \approx 5$ mm. Depending on the smallest feature in the image, this could be too high. For example, such level of blur would be ten times higher than a typical cooling hole overall dimension (0.5 mm). To quantify the blur in pixel, knowledge of working distance, pixel size, and focal length is required. A significantly short integration time would reduce blurring and allow detection of smallest features such as cooling holes. However, minimising the integration time decreases saturation and increases signal-to-noise ratio, possibly leading to significant measurement error. As the target temperature increases so does the detector saturation, allowing a reduction of the integration time for the same signal-to-noise ratio.

The relationship between target temperature, integration time and detector saturation and the implications on the measurement error needs to be fully investigated to understand this limit and select the appropriate integration time. To this purpose, the detector calibration was performed and studied over a range of integration times from 5 µs to 70 µs. For context, for a typical tangential blade velocity of 250 m/s in the OTRF, integration times of 5 µs and 70 µs would theoretically result in motion blur of 1.25 mm and 17.5 mm respectively.

A typical set of calibration data for a single pixel are shown in Fig. 6. Fig. 6(a) shows the temperature as a function of the recorded signal in digital counts for different integration time. The detector saturation lower and upper limits recommended by the camera manufacturer are represented on the graph by vertical dashed lines, with values of 12% and 82% respectively. These suggest what combination of integration time and target temperature is recommended for each specific case. For example, for temperatures between ambient and 363.15 K, it is recommended to set the integration time above 50 µs, which corresponds to a detector saturation of 23% at 363.15 K and 11% at 293.15 K. At elevated temperatures, the minimum integration time can be reduced. For instance, temperatures exceeding 373.15 K permit an integration time of 20 µs, those exceeding 423.15 K allow for 10 µs, while for temperature higher than 513.15 K an integration time of 5 µs is permitted. Fig. 6(b) shows the radiance as a function of the digital counts. This plot shows how the detector behaviour remains linear across the entire temperature range, even at the lowest integration time tested.

In the OTRF rotor speeds of 7500–9500 rpm are typical to achieve representative test conditions. In a cooled experiment, surface temperatures below 373.15 K are expected in regions of high cooling effectiveness. With such high rotor speeds, a minimum integration time is desirable to minimise blur, resulting in likely undersaturated measurements at lower surface temperatures. Hence, it is fundamental to understand the implications of working in the undersaturated detector region and how this translates into measurement errors.

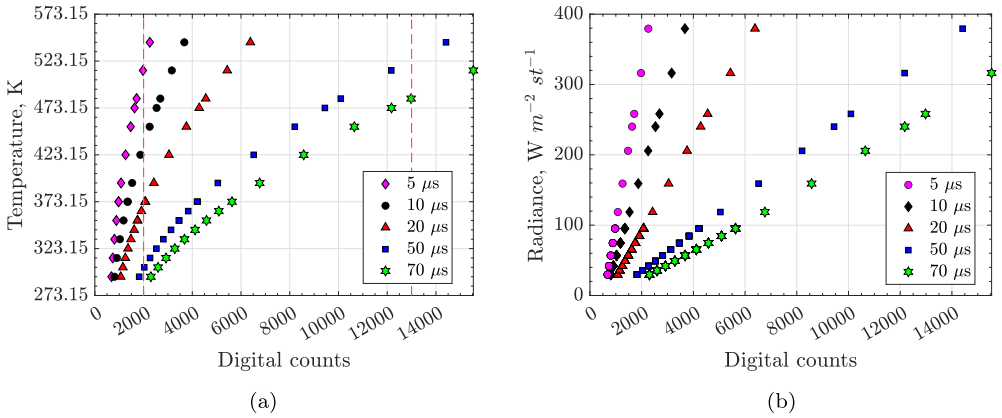

Fig. 6. (a) Blackbody equivalent temperature and (b) Radiance as a function of digital counts, for five integration times.

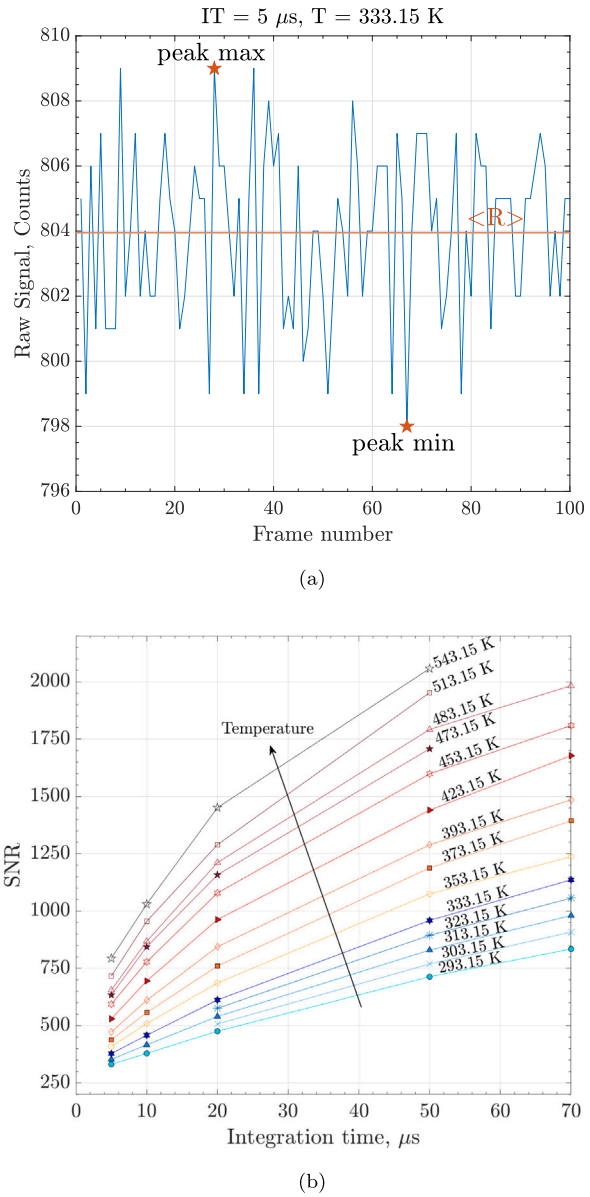

Fig. 7. (a) Raw signal from a randomly selected pixel, 100 frames acquired at 125 Hz, integration time of 5 µs and temperature of the blackbody source set at 333.15 K (b) Signal-to-Noise Ratio as a function of integration time and blackbody source temperature.

The signal to noise ratio (SNR) noise was evaluated over a range of blackbody temperature and integration time. Data were acquired over 100 frames and across the FPA. An example of the temporal signal of a randomly selected pixel acquired during a calibration is shown in Fig. 7(a). The calculated SNR is plotted in Fig. 7(b) as a function of integration time and blackbody temperature. As expected, SNR increases with both variables. An increase in both variables results in more energy, and hence a higher signal, to be recorded by the camera, causing an increase in SNR.

Typical temperature readings with $T_{bb} = 313.15\,\mathrm{K}$ for a range of integration times are shown in Fig. 8(a). Black lines indicate the mean temperature reading over the 100 frames, while red lines indicate the reference blackbody source temperature. Moving from the shortest to the longest integration time both the standard deviation and error in the mean value become smaller. This can be further inferred from Fig. 8(b), showing the absolute error defined as the difference between the real target temperature and the camera reading. The error fluctuates by approximately $\pm 1\,\mathrm{K}$ (2σ) around a mean of 1 K for $IT = 5\,\mu\mathrm{s}$. The fluctuation range reduces to $\pm 0.1\,\mathrm{K}$ around a mean of 0.07 K for $IT = 70\,\mu\mathrm{s}$. Finally, Fig. 9 depicts the maximum error in temperature reading as a function of integration time and temperature of the blackbody source from one randomly selected pixel. Such plot enables the user to make an informed decision regarding the choice of integration time. If very high accuracy is required, it might not be possible to use a low integration time to minimise the blur, and hence image processing techniques are required to compensate for this limitation.

2.2. Surface emissivity calibration

Accurate knowledge of target surface emissivity is a fundamental step to achieve high-accuracy IR thermography measurements. Typical emissivity values are readily available for a range of materials, however the influence of surface condition and viewing angle on emissivity should be considered. The set-up and calibrator used for evaluating the emissivity have been described in the previous section and are depicted in Fig. 4b and c. Calibrations were performed over a range of target thermocouple temperature, T_{TC}, between 303.15 K and 373.15 K.

Two methods were used and compared for evaluating surface emissivity, both assuming an air transmittance equal to unity [20]. The first method solves Eq. (1) for emissivity, obtaining the following:

$$\varepsilon(\theta) = \frac{T_{cam}^4(\theta) - T_r^4}{T_{TC}^4 - T_r^4} \tag{5}$$

The reflected temperature of the surroundings, T_r, is kept at the same level as the ambient temperature during the experiments and is measured by a K-type thermocouple.

The second method used to evaluate the surface emissivity requires two sets of data (test 1 and test 2) acquired at different target temperatures, and it is based on the assumption of consistent surroundings

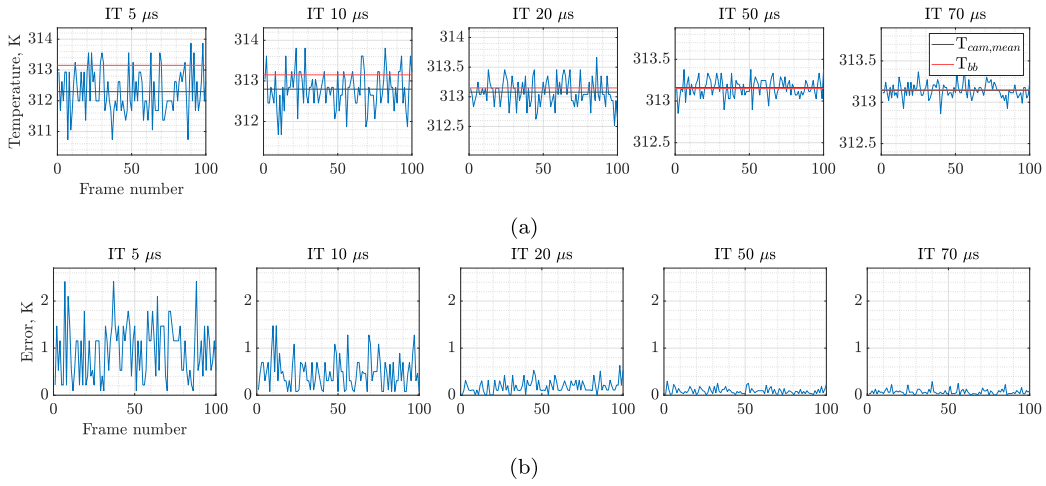

Fig. 8. (a) Equivalent blackbody temperature reading T_{cam} and (b) absolute error in temperature reading from a randomly selected pixel, for 100 frames acquired at 125 Hz. Range of integration times from 5 μs to 70 μs.

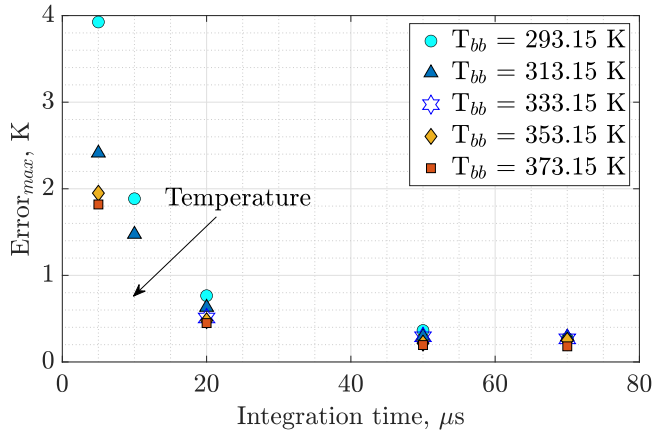

Fig. 9. Maximum absolute error in temperature reading T_{cam} of a random selected pixel as a function of integration time, for temperature between 293.15 K and 373.15 K.

conditions, and hence T_r. From the energy balance, it is possible to obtain two equations in two unknowns: ε and T_r. The equations solved for ε give:

$$\varepsilon(\theta) = \frac{L(T_{cam,test2}) - L(T_{cam,test1})}{L(T_{TC,test2}) - L(T_{TC,test1})} \tag{6}$$

where $L(T)$ are the radiances calculated from the temperature by integrating Planck's equation.

A typical temperature map for a steady target temperature T_{TC} = 364.15 K, obtained applying the detector calibration is shown in Fig. 10(a) (all 8 thermocouples measured within ±0.3 K of mean). The highlighted areas A, B, C, D were used to evaluate the emissivity of the RS black matt paint, due to their proximity to thermocouple locations. The area labelled AL was covered by aluminium tape and was used as a reference for the emissivity calculation for this material.

The emissivity maps for the paint (sector D) and the aluminium tape (sector AL) calculated with the first method are shown in Fig. 10(b). Surface emissivity values of 0.938 ± 0.007 and 0.040 ± 0.004 were calculated respectively.

The emissivity values for the paint obtained using Eqs. (5) and (6) as a function of target temperature are shown in Fig. 11. The two methods agree at higher target temperatures with emissivity values of 0.94. What appears to be an emissivity temperature dependence in Fig. 11(a) can be explained by measurement errors at low temperature. For target temperature close to T_r even small measurement errors, typically 0.4% for a T-type thermocouple conforming to IEC-584-2 standards with a class 1 tolerance [21], translate into a significant error in the emissivity calculation. Both methods are valid, however, care should be taken with the first method to ensure a large enough temperature difference between T_{TC} and T_r to minimise measurement error. Results suggest a temperature difference of at least 60 K is required.

The calibration of the directional emissivity for the high emissivity paint was conducted across a range of 0-deg to 75-deg, with the corresponding trend depicted in Fig. 12. The calibrator was rotated to adjust the angle with respect to the camera, and the measurements conducted following the aforementioned methodology. It was observed that the emissivity remains almost constant and equivalent to the normal emissivity (ε = 0.94) up to angles of 50-deg. Subsequently, it gradually decreases and reaches a value of 0.83. This is in general agreement with previous results in literature [22].

When performing infrared measurements within turbine facilities, knowledge of viewing angles alongside the directional emissivity calibration curve becomes essential to assign the correct value of emissivity for each scenario. This involves two key aspects: the computation of anticipated viewing angles and the strategic alignment of the camera to ensure angles below 50-deg in areas of significance. To address this, a Matlab code was developed for evaluating viewing angles in the OTRF. Target surface normals are derived from an imported surface mesh of turbine and camera 3D geometry, with viewing angles subsequently determined by the vector dot product calculations. After iterating various camera-target positions, three were found with observation angles below ±50-deg in the regions of measurement, i.e. rotor tip, near-tip pressure and suction sides. Fig. 13 shows the turbine sector CAD with the camera (mounted in three positions), optical window and rotor blades. The calculated viewing angles on the blade tip, pressure and suction surfaces for these camera positions are shown in Figs. 13(b), 13(c) and 13(d), respectively. This procedure not only provides insight into viewing angles but also allows informed selection of directional emissivity.

2.3. Transmittance calibration

Characterisation of the optical path in terms of transmittance is also required to accurately evaluate the target temperature. Within the OTRF, the path consists of dry air at temperature ranging from 400 to 600 K, as well as a ZnSe optical window coated with anti-reflective. According to Gao et al. [20], the gas transmittance can be assumed equal to unity for wavelength above 7 μm, and hence the transmittance of the window alone needs to be determined. Given the short duration of the test in the OTRF (0.5 s) and the window material

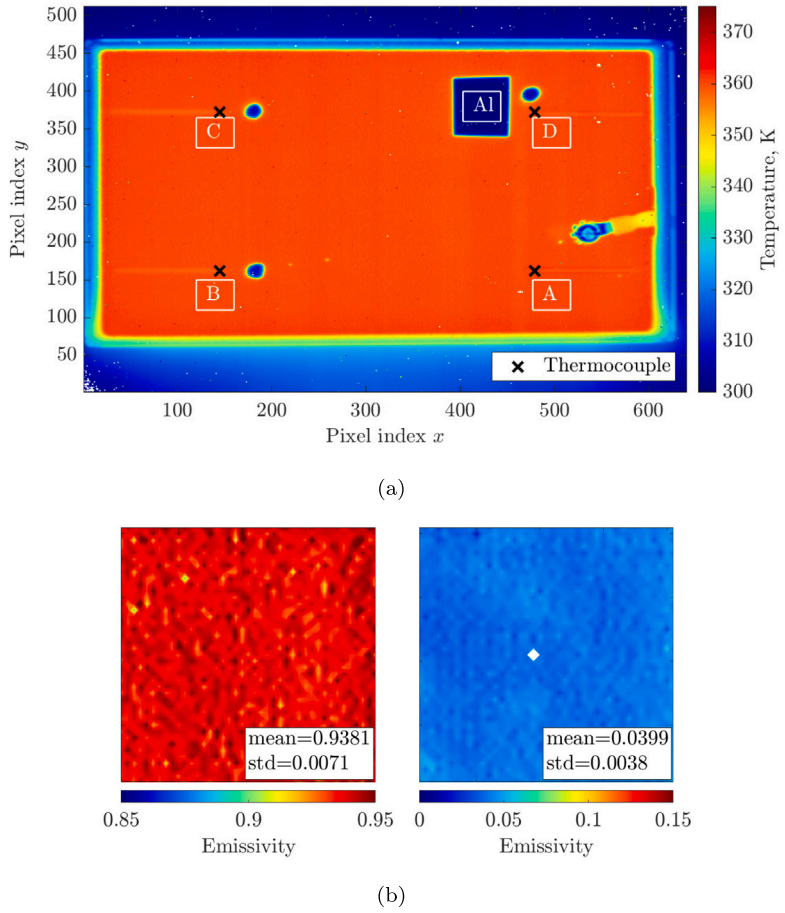

Fig. 10. (a) Processed image of T_{cam} of the calibrator surface. The letters A, B, C, D indicate the regions used to evaluate the emissivity. Black crosses indicate the locations of the embedded thermocouples. (b) Emissivity maps for RS matt black paint (region D) and aluminium tape (AL).

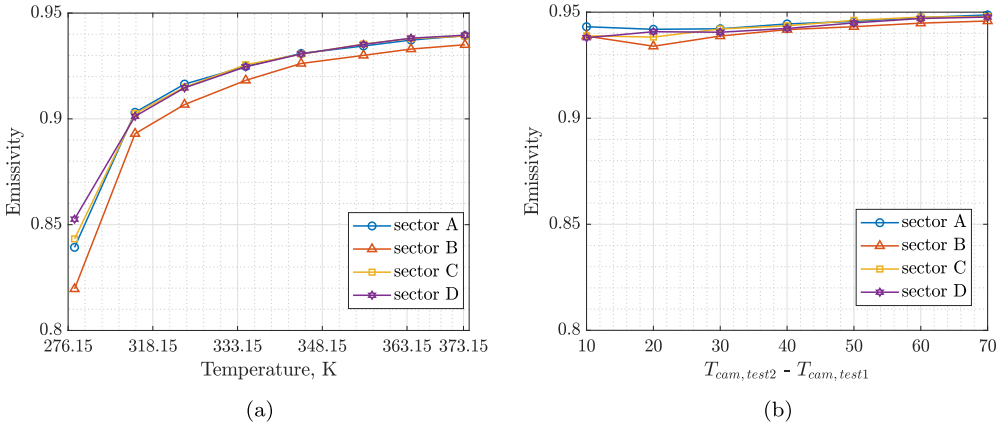

Fig. 11. Emissivity ε of the black matt coating obtained (a) using Eq. (5) and (b) Eq. (6).

properties [23], the window temperature increase has a negligible impact on the transmittance of the window [24]. The transmittance of the ZnSe was determined by placing the optical window between the blackbody source and the camera in the calibration set-up depicted in Fig. 4a, replicating the same geometrical conditions expected in the OTRF for experiments with focus on blade tip (Fig. 13(b)). Calibration investigations as a function of viewing angle are required for non-uniform thickness window geometries.

Using the temperature measured by the camera, T_{cam}, the blackbody source temperature, T_{bb}, and the optical path temperature, T_{opt}, the transmittance was calculated by rearranging Eq. (1) as:

$$\tau = \frac{T_{cam}^4(\theta) - T_{opt}^4}{T_{bb}^4 - T_{opt}^4} \tag{7}$$

The optical path temperature is kept at the same level as the ambient temperature during the experiments and is measured by a K-type thermocouple.

The transmittance tested for blackbody source temperatures ranging from 323.15 K to 343.15 K was determined to be $\tau = 0.95$.

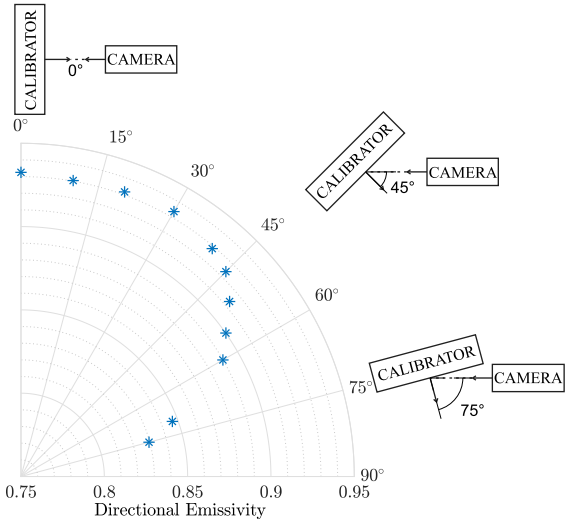

Fig. 12. Polar plot of the measured directional emissivity.

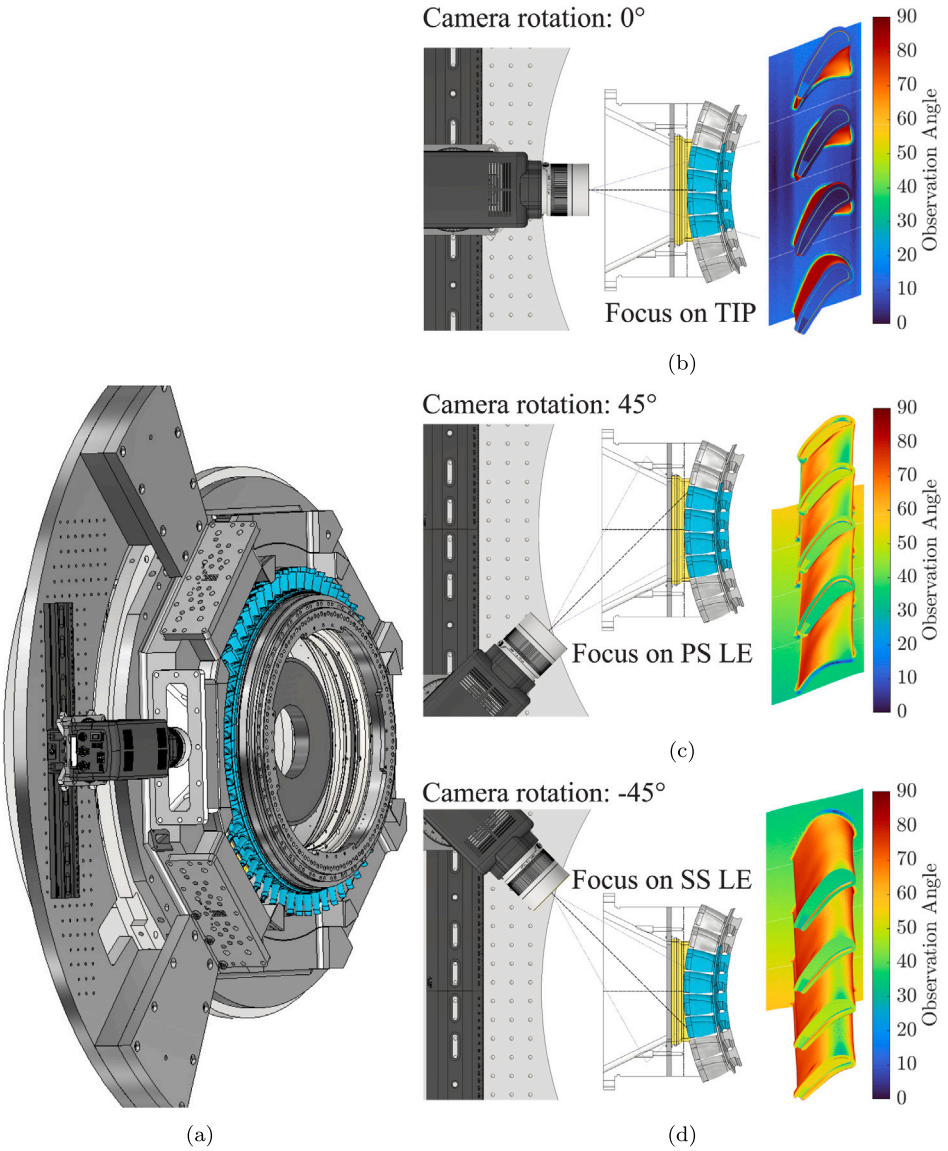

Fig. 13. (a) 3D CAD geometry of the OTRF test section showing the camera support system. Observation angle on the rotor blades at camera rotation of (b) 0-deg with focus on rotor blade tip; (c) 45-deg with focus on pressure side (PS); (d) −45-deg with focus on suction side (SS).

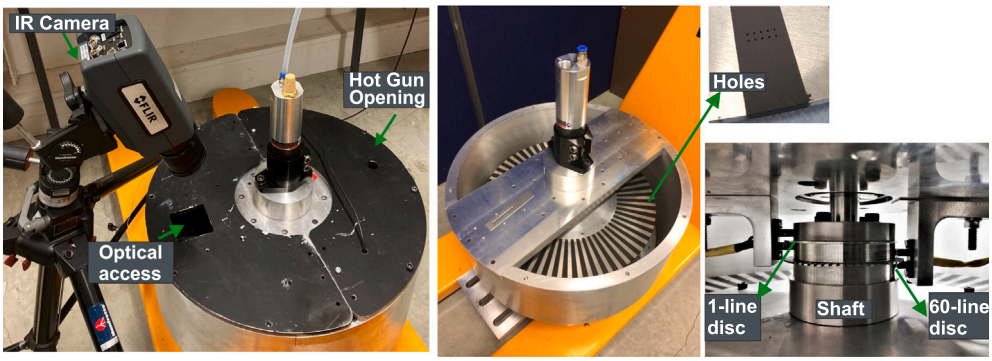

Fig. 14. Rotating facility, with a close-up of the encoder installation (right bottom) and cooling holes of 0.5 mm diameter (right top) [16].

2.4. Reflection calibration

The disturbance radiation originating from reflections from the target surface provides the most challenging calibration as it depends on geometry and temperature distribution of the environment. Some studies have considered it constant [3–5], and generally, it is advised to calibrate for this disturbance in situ [6,7]. The method presented developed the technique proposed by Kirollos and Povey [7] with the additional allowance of the optical path transmittance. The method is based on the concept that two isothermal regions of the target, each with a different surface emissivity, will radiate different magnitudes of total, emitted and reflected radiation. If the surface emissivity for each region is known, the true target and reflected temperatures can be found applying Eq. (1) to the measurements from each region:

$$T_t^4 = \frac{1-\varepsilon_2}{\tau(\varepsilon_1-\varepsilon_2)}T_{cam1}^4 - \frac{1-\varepsilon_1}{\tau(\varepsilon_1-\varepsilon_2)}T_{cam2}^4 - \frac{1-\tau}{\tau}T_{opt}^4 \tag{8}$$

$$T_r^4 = \frac{\varepsilon_1}{\tau(\varepsilon_1-\varepsilon_2)}T_{cam2}^4 - \frac{\varepsilon_2}{\tau(\varepsilon_1-\varepsilon_2)}T_{cam1}^4 - \frac{1-\tau}{\tau}T_{opt}^4 \tag{9}$$

where subscript 1 refers to region 1, while subscript 2 refers to region 2.

The ultimate goal of the paper is to develop a calibration procedure for a rotating set-up; initially however, the method was applied to the emissivity calibrator shown in Fig. 4b and c as proof of concept. A disturbance to enhance the reflections level was introduced by placing a hot soldering iron in proximity of the target. Results for an experimental temperature $T_{TC} = 335.8$ K are summarised in Table 2. Zones D and AL on the calibrator (see Fig. 10(a)) were used as high emissivity and low emissivity regions, where the recorded blackbody equivalent temperatures were 332.8 K and 296.7 K, respectively. Thus, the measurement errors before the correction, $\Delta_1 = T_{cam} - T_{TC}$, were −3 K and −39.1 K, respectively.

Applying corrections for surface emissivity and reflection according to Eqs. (8) and (9), a reflected temperature, T_r, of 294.75 K, and a target temperature, T_t, of 334.8 K were calculated. Thus, the calibration procedure was able to reduce the measurement error to within the thermocouple accuracy, from 3 K (0.9%) to 1 K (0.3%). Considering the results presented in Fig. 2, it is clear that the regions of high and low surface emissivity provide accurate measurement of T_t and T_r respectively, allowing accurate correction to the true target temperature.

The relative magnitudes of surface emissivity and reflection corrections can be estimated by correcting for the target emissivity alone, i.e. applying Eq. (1) with $T_r = 0$. In the high emissivity region, this results in a corrected temperature, $T_t' = T_{cam}/\varepsilon^{1/4} = 337.98$ K. Hence, it is estimated that the surface emissivity and reflection corrections were same order of magnitude at +5.18 K(+1.55%) and −3.18 K(−0.95%) respectively, providing evidence of accurate correction for both sources of error.

Table 2
Emissivity and reflection correction applied to an experimental case.

ε	T_{TC}	T_{cam}	Δ_1	T_t'	Δ_2	T_t	T_r	Δ_3
0.94	335.8	332.8	−3.0	337.98	2.18	334.8	294.75	−1
0.04	335.8	296.7	−39.1			334.8	294.75	−1

3. Calibration performance on high-speed objects

The IR system capability to measure temperature of a high-speed rotating target was assessed in an experimental set-up that comprises a 450 mm diameter aluminium disc made of 6082 T6 alloy, as shown in Fig. 14. An electrical motor drives the disc at a maximum speed of 4000 rpm (equivalent to approximately 66 Hz). The rotating disc is enclosed within a cylindrical chamber, with a square-shaped opening on the top cover to enable optical access. The disc is heated using a hot air blower whilst spinning, with the enclosure air temperature monitored with a K-type thermocouple. RS Matt Black paint was applied to the disc to create a pattern that emulates the passage of 60 rotor blades, with two stripes featuring an array of holes to represent film cooling holes of 0.5 mm diameter. A 1-line optical encoder signal indicates the disc rotational speed (rpm), whilst a 60-line optical encoder enables phase lock image acquisition of the desired stripe (see Fig. 14).

The aim of the experiments is to examine the degree to which velocity and blur affect the calibration procedure presented in the previous sections. Tests were performed up to 4000 rpm, corresponding to a tangential velocity of approximately 100 m s^{-1}, with integration times of 20 µs and 70 µs. Typical infrared measurements of equivalent blackbody temperature T_{cam} are shown in Fig. 15 for data acquired at 1500 rpm and 3000 rpm for both integration times. A few qualitative observations can be inferred from these results: (i) the importance of high emissivity coating to minimise disturbance radiation is undeniable. The reflections from the optical access are clear in all images ($400 < y < 500$ & $160 < x < 450$). The areas with low emissivity, corresponding to the radial stripes of low T_{cam}, are clearly disturbed by the reflections whilst little difference is visible in the regions of high emissivity; (ii) the set-up presents an intrinsic radial temperature distribution caused by the heating targeted at the disc outer radius; (iii) reducing integration time provides an image with sharper edges for a constant target velocity; (iv) measurement noise increases as integration time is decreased, indeed the shorter integration time limits the amount of infrared radiation detected; the phenomenon is evident as a non uniform signal even on the high emissivity regions, particularly visible for the data taken at $N = 3000$ rpm with 20 µs integration time on the central stripe. These observations agree with the results demonstrated previously in the steady calibration facility.

3.1. Emissivity and reflections correction with blur

In this section the effect of rotation and motion blur on measurement accuracy is evaluated in detail. Figs. 16(a) and 16(b) show

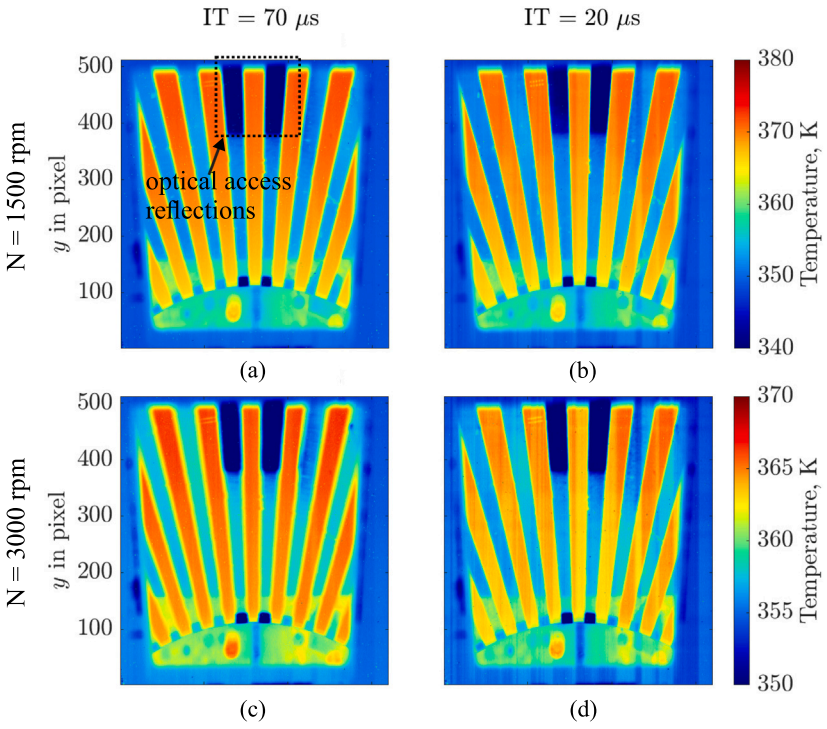

Fig. 15. Processed images of T_{cam} at different camera integration time (IT) and disc speed (N): (a) IT = 70 μs and $N = 1500$ rpm, (b) IT = 20 μs and $N = 1500$ rpm, (c) IT = 70 μs and $N = 3000$ rpm (d) IT = 20 μs and $N = 3000$ rpm.

the processed images of the blackbody equivalent temperature T_{cam} acquired at $N = 0$ rpm and $N = 3000$ rpm respectively. Figs. 16(c) and 16(d) depict the blackbody equivalent temperature at $y = 480$ pixel and $47 < x < 569$ pixels (range indicated with *line* in Fig. 16). The different regions are displayed: high emissivity regions (painted part) and low emissivity regions (metallic uncoated part) alternate, with zones of blur in between for the rotating test case. The blur regions are identified by thresholds Edge 1 and Edge 2. These are defined as the temperature where the tangent to the camera signal changes. It can be inferred from Fig. 16(c) that in absence of blur ($N = 0$ rpm), the signal is more similar to a square wave, where the non-perfect vertical slope is down to the variable paint thickness at the stripe borders, which in turns impacts the surface emissivity.

The reflections calibration requires the division of the two regions to obtain T_{cam1} (high emissivity region) and T_{cam2} (low emissivity region). Interpolation is then required to obtain the information across the entire FOV for both signals. In the case of a steady target this is a straightforward task, as a simple edge detection would suffice. However, this becomes more challenging in the case of moving target due to the presence of blur. Three edge detection methods were trialled:

Method 1: The blur region was completely removed from the analysis. The high emissivity region and low emissivity regions were identified as follows: $T_{cam1} = \{T_{cam}(x,y) \parallel T_{cam}(x,y) \geq Edge1\}$

$T_{cam2} = \{T_{cam}(x,y) \parallel T_{cam}(x,y) \leq Edge2\}$.

Method 2: The blur was incorporated into the high emissivity region. The high emissivity region and low emissivity regions were identified as follows: $T_{cam1} = \{T_{cam}(x,y) \parallel T_{cam}(x,y) \geq Edge2\}$

$T_{cam2} = \{T_{cam}(x,y) \parallel T_{cam}(x,y) \leq Edge2\}$.

Method 3: The blur was incorporated into the low emissivity region. The high emissivity region and low emissivity regions were identified as follows: $T_{cam1} = \{T_{cam}(x,y) \parallel T_{cam}(x,y) \geq Edge1\}$

$T_{cam2} = \{T_{cam}(x,y) \parallel T_{cam}(x,y) \leq Edge1\}$.

A Region of Interest (ROI) was defined on the camera temperature map ($T_{cam}(x,y)$), as shown with a dashed line in Fig. 16(b). Subsequently, the signals T_{cam1} and T_{cam2} were identified by using the methods described above, obtaining Fig. 17(a) with method 1, Fig. 17(b) with method 2, and Fig. 17(c) with method 3. Having observed the intrinsic radial temperature distribution of the rig, the interpolation of T_{cam1} and T_{cam2} was carried out radially. Finally, Eqs. (8) and (9) were used to calculate the target temperature and the reflected temperature from the camera signal.

The calibrated signal $T_t(x,y)$ and the reflected temperature $T_r(x,y)$ are shown in Figs. 18(a), 18(b), 18(c) for the respective edge detection methods. For all methods, T_t is found to be higher than T_{cam}. This can be explained by observing that the target is hotter than the surroundings ($T_t = 366$ K, while $335 < T_r < 360$ K), which therefore have the effect of lowering the signal reaching the camera.

With removal of the blurred region from the assessment of T_{cam1} and T_{cam2} (*method 1*), the target temperature was successfully reconstructed across the entire area. An approximately constant temperature distribution resulted, with almost no disturbance between the low and high emissivity regions (no border effects on the regions affected by reflections). This calibration method provided the best reconstructed signal. This can be further confirmed by comparing the calibrated target temperature and the camera temperature at locations $y = 311$ and $y = 480$ presented in Figs. 19 and 20 respectively. The two locations were chosen to show how the calibration performs in the ideal instance of constant reflection signal, as for $y = 311$, and in the instance of strongly spatial dependent reflection signal, as for $y = 480$ where the presence of the window causes the outside environment to affect the measurement.

The calibration carried out by attributing blurred data to T_{cam1} (*method 2*) effectively calibrated the high emissivity signal, however it struggles to achieve the same degree of accuracy in the low emissivity region. The temperature difference between the high-emissivity region and the low emissivity region is approximately 2 K, see Figs. 19(b) and 20(b). In addition, a clear border effect was found in the blur region with a maximum temperature difference between the high and low

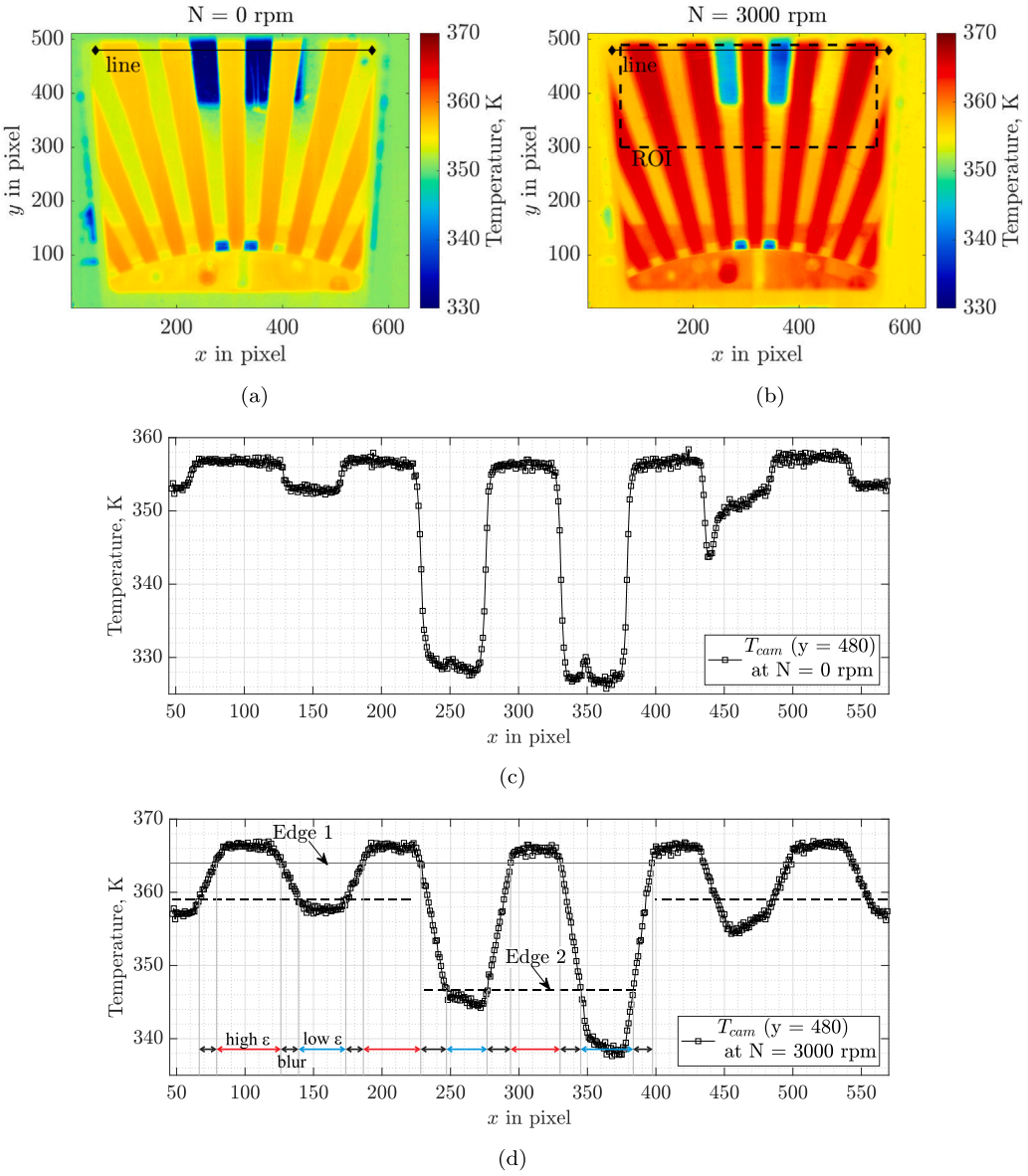

Fig. 16. Processed images of T_{cam} for test conditions: (a) IT = 70 µs and N = 0 rpm, and (b) IT = 70 µs and N = 3000 rpm. Corresponding temperatures over a line for (c) IT = 70 µs and N = 0 rpm (location y = 480) and (d) IT = 70 µs and N = 3000 rpm (location y = 400).

emissivity regions of 7 K at location $y = 311$ and of approximately 20 K at location $y = 480$.

The calibration carried out by attributing the blurred region to T_{cam2} (*method 3*) performs almost as well as by removing the blurred region (*method 1*). Nevertheless, a non-real parabolic temperature profile is found. The temperature difference between the high-emissivity region and the low emissivity region is approximately 0.5 K. The border effect is still being visible, however its magnitude is reduced to a maximum temperature difference of 1 K at both locations $y = 311$ and $y = 480$.

Having concluded that calibrating using *method 1* gives the most realistic signal, a true target temperature was defined for each radius by radially averaging the signal obtained with this correction: $T_{tt}(y) = \sum_x T_{t,method\,1}(x, y)$. It was therefore possible to define the error resulting from blur as the difference between the true target temperature and the temperature obtained with the post-calibration, as follows:

$$Error, \% = \frac{T_{tt}(y) - T_{t,calib}(x, y)}{T_{tt}(y)} \cdot 100 \tag{10}$$

The errors at location $y = 311$ and $y = 480$, are shown in Fig. 21. As expected, the highest errors appear when *method 2* is used to calibrate the signal. By including the blur into the high emissivity region, the residual error in the low emissivity region is of 0.5%, while in the blur region the error goes from 0.5% to 1.7% at $y = 311$ and from 0.5% to 7% at $y = 480$. Lower error levels are found with the use of *method 3*, where the error ranges from 0% to 0.2% at both locations $y = 311$ and $y = 480$.

The results show that careful considerations need to be taken before applying the calibration to blurred images. The first edge detection presented removed completely the blur from the analysis, and the method was successful in calibrating the target signal.

In the Oxford Turbine Research Facility, measurements of reflected temperature will be acquired from a blade with low emissivity. The challenges of image deblurring to capture features such as cooling holes sit outside of the main focus of the paper and are going to be addressed in future publications.

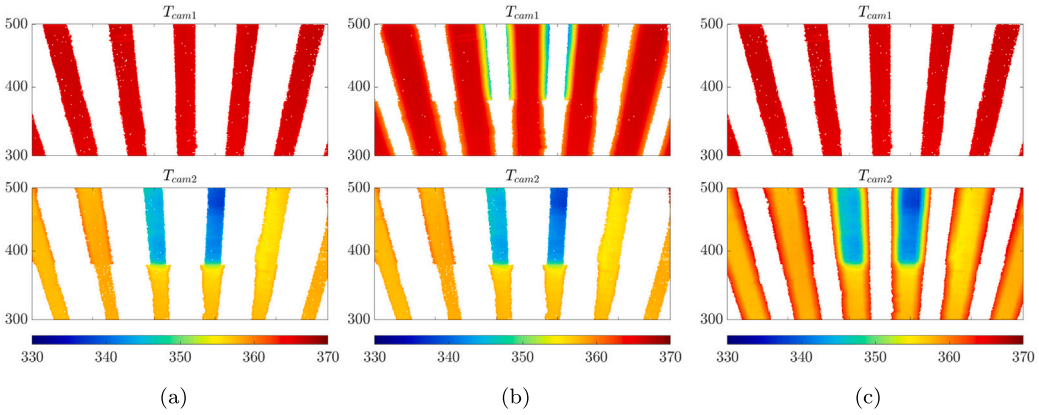

Fig. 17. Camera signals divided into T_{cam1} and T_{cam2} by using (a) Method 1, (b) Method 2, and (c) Method 3.

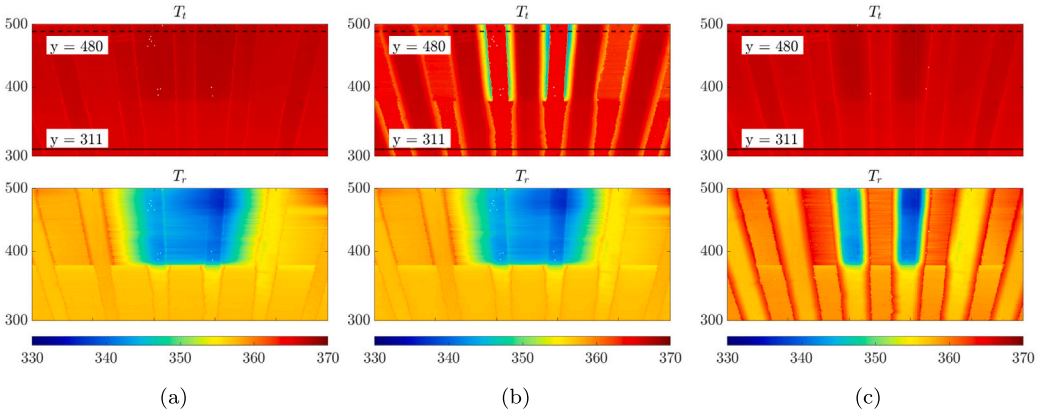

Fig. 18. Target and reflected temperature, T_t and T_r, obtained with (a) Method 1, (b) Method 2 and (c) Method 3.

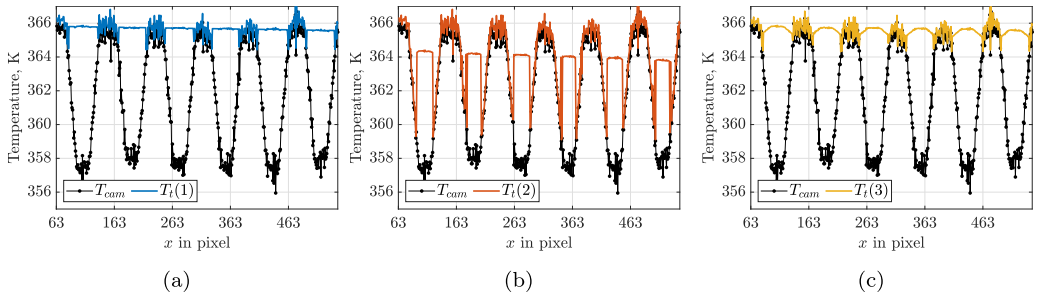

Fig. 19. Camera and calibrated signals at location $y = 311$ obtained using (a) Method 1, (b) Method 2, and (c) Method 3.

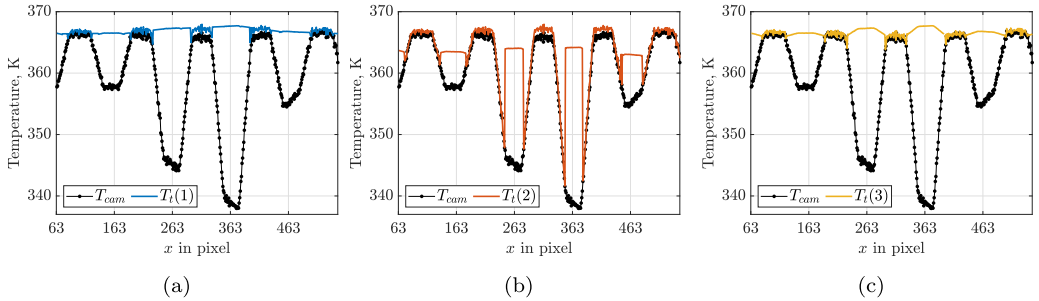

Fig. 20. Camera and calibrated signals at location $y = 480$ obtained using (a) Method 1, (b) Method 2, and (c) Method 3.

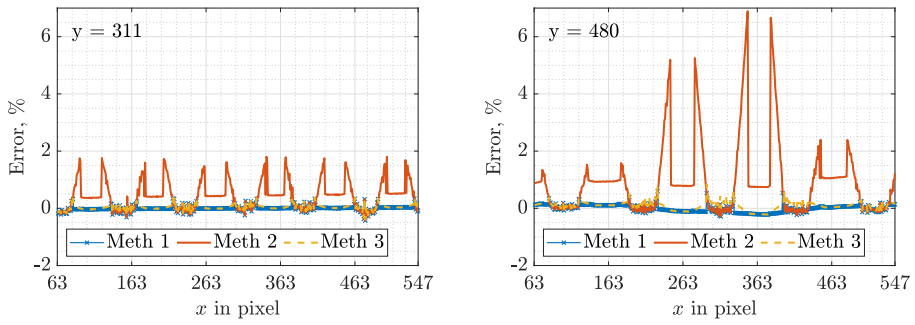

Fig. 21. Errors after calibration at locations (a) y = 311; (b) y = 480.

Table 3
Calibration uncertainty analysis, assuming $\tau = 0.95$, $\epsilon = 0.95$, $T_r = 298\,\text{K}$, $T_{opt} = 298\,\text{K}$.

Detector					
		323.15 K	373.15 K	423.15 K	473.15 K
$U_{T_{bb}}$	Blackbody calibrator, K	±1.65	±1.99	±1.84	±1.82
$U_{fitting}$	rmse, K	±0.15	±0.18	±0.18	±0.18
$U_{T_{cam}}$	IR camera, K	±1.65	±2.00	±1.84	±1.82
Emissivity					
		323.15 K	373.15 K	423.15 K	473.15 K
$U_{T_{cam}}$	IR camera, K	±1.65	±2.00	±1.84	±1.82
$U_{T_{TC}}$, U_{T_S}	T-type thermocouple, K	±1.29	±1.49	±1.69	±1.89
U_ϵ	Emissivity	±0.02	±0.01	±0.01	±0.01
Transmittance					
		323.15 K	373.15 K	423.15 K	473.15 K
$U_{T_{cam}}$	IR camera, K	±1.65	±2.00	±1.84	±1.82
$U_{T_{bb}}$	Blackbody calibrator, K	±1.65	±1.99	±1.84	±1.82
$U_{T_{opt}}$	T-type thermocouple, K	±1.29	±1.49	±1.69	±1.89
U_τ	Transmittance	±0.01	±0.01	±0.01	±0.01

Table 4
Target temperature uncertainty analysis, assuming $\tau = 0.95$, $\epsilon_1 = 0.94$, $\epsilon_2 = 0.04$, $T_r = 550\,\text{K}$, $T_{opt} = 430\,\text{K}$.

		323.15 K	373.15 K	423.15 K	473.15 K
$U_{T_{cam1}}$, $U_{T_{cam2}}$	IR camera, K	±1.65	±2.00	±1.84	±1.82
$U_{\epsilon 1}$, $U_{\epsilon 2}$	Emissivity	±0.02	±0.01	±0.01	±0.01
U_τ	Transmittance	±0.01	±0.01	±0.01	±0.01
U_{T_t}	IR calibration, K	±14.0	±5.30	±3.14	±2.36
U_{T_t}	IR calibration, %	4.35	1.42	0.74	0.50

Table 5
Metal effectiveness uncertainty analysis.

T_t	Blade temperature	373.15 K	398.15 K	423.15 K	448.15 K	473.15 K
η	Metal effectiveness	0.55	0.41	0.27	0.14	0
U_η	Metal effectiveness	±0.03	±0.02	±0.01	±0.01	±0.01

4. Quantifying uncertainty in target temperature and metal effectiveness

The uncertainty analysis of the calibration procedure to determine the target temperature T_t are summarised in Tables 3 and 4.

The results of the uncertainty analysis are obtained for four target temperatures, between 323.15 K and 473.15 K. The analysis is divided into: detector calibration, emissivity calibration, transmittance calibration, and target temperature. The uncertainty associated with the detector calibration, $U_{T_{cam}}$, arises from the combined errors in the reference blackbody source, $U_{T_{bb}}$, and the error from the fourth order polynomial fitting, $U_{fitting}$, which has second order influence. The uncertainty in the directional emissivity, U_ϵ, and transmittance, U_τ, stem from error propagation associated with Eqs. (5) and (7), respectively. Uncertainty on reference thermocouples were taken from manufacturer specifications. Both errors reduce as target temperature increases.

To evaluate the uncertainty in the target temperature, as calculated from Eq. (8), expected values in the OTRF were used: $T_{opt} = 430\,\text{K}$ and $T_r = 550\,\text{K}$, $\tau = 0.95$, $\epsilon_1 = 0.94$, $\epsilon_2 = 0.04$. The uncertainty in the calculated T_t arises from the propagation errors of the previously listed errors. Based on the analysis, target temperature errors range from ±14 K (4.35%) for $T_t = 323.15\,\text{K}$, to ±2.36 K (0.5%) for $T_t = 473.15\,\text{K}$, in absolute terms. The higher error for $T_t = 323.15\,\text{K}$ arises from the combination of low target temperature and high reflected temperature. Indeed, if a reflected temperature of $T_r = 298\,\text{K}$ was used the uncertainty calculation would range from ±2.85 K for $T_t = 323.15\,\text{K}$, to ±1.43 K for $T_t = 473.15\,\text{K}$. It is noted that the two results differ mostly for very low target temperatures.

The main purpose of the IR measurement system is to assess cooling and metal effectiveness in the OTRF. Metal effectiveness provides a non-dimensional surface temperature scalable to engine conditions, and it is defined as:

$$\eta = \frac{T_g - T_t}{T_g - T_c} \tag{11}$$

The target temperature, T_t, is calculated according to Eq. (2), T_c and T_g are coolant and gas temperatures, respectively, equal to $T_c = 290\,\text{K}$ and $T_g = 473\,\text{K}$.

The computed uncertainties in the measurement of metal effectiveness, η, were evaluated for blade temperatures between 100–200 °C. The results presented in Table 5 were obtained using typical uncertainty in coolant and inlet gas temperatures of ±1 K and ±2.5 K, respectively. The bias error in η ranges from ±0.03 to ±0.01, in absolute terms. It is noteworthy that precision (or repeatability) errors, which indicate the capability of the measurement system to detect variations in metal effectiveness due to variations in turbine operational conditions or in blade cooling technologies, have not been considered in this preliminary analysis as they are anticipated to be significantly smaller than the reported bias errors.

5. Conclusion

A novel method to calibrate and perform high-accuracy infrared measurements on high-speed targets in the Oxford Turbine Research Facility has been developed. Nevertheless, the method is extendable to any application, in particular to situations where an in situ calibration is impracticable.

The camera detector was calibrated pixel-by-pixel at various integration times, ranging from 5 µs to 70 µs, against traceable blackbody sources with a maximum uncertainty of ±0.5% of the target temperature. Analysis of the signal-to-noise ratio, as a function of integration time and blackbody equivalent temperature, highlights the significance of accurately assessing the combination of signal intensity and integration time to ensure minimal noise effects.

A bespoke facility was developed to accurately characterise directional emissivity and transmittance; both to within ±0.01. Two post-test analysis methods to assess surface emissivity calibration methods were presented. For accurate results, appraisal utilising the first method must be performed with a significant temperature difference between the target and surroundings. A temperature difference of at least 60 K is recommended. Appraisal utilising the second method requires data at two different target temperatures and displays results that are invariant with target temperature as expected.

To understand the impact of motion blur, a reflection calibration method was tested in a rotating facility. Three different corrections for blur were presented: the first artificially eliminates the motion blur before the correction, while the second and the last incorporate the blur in the high-emissivity and low-emissivity region respectively. The first correction is the only method that successfully calibrated the signal across the entire Field of View. However, in experiments with highly spatial temperature variation, removing data would reduce the spatial resolution of the technique, potentially leading to higher errors. In such situations, applying deblurring techniques prior to calibration is recommended.

The results from the calibration outlined demonstrate that the absolute uncertainty on the target temperature varies from ±5.30 K at $T = 373.15$ K to ±2.36 K at $T = 473.15$ K. These would translate into an uncertainty in metal effectiveness of approximately ±0.03 and ±0.01, respectively — equivalent to a real engine metal temperature variation of ±7 K, significantly smaller than the resolution of modern thermal paints. Subsequently, the presented approach is expected to yield valuable and accurate heat transfer and metal effectiveness data, which will aid in the development of more efficient gas turbine components and cooling technologies.

Nomenclature

Abbreviations	
FOV	Field of View
IR	Infrared
IT	Integration time of the camera
NUC	Non-Uniformity Correction
OTRF	Oxford Turbine Research Facility
SNR	Signal to Noise Ratio
ZnSe	Zinc-Selenide material
Roman letters	
C	Influence coefficient
R	Pixel digital count
T	Temperature, K
U	Uncertainty
Greek letters	
η	Metal effectiveness
ϵ	Emissivity
τ	Transmittance
θ	Observation angle
Subscripts	
bb	Blackbody
c	Coolant
cam	Camera (equivalent blackbody)
$corr$	Corrected
g	Gas
i	Blackbody source temperature
opt	Optical path
r	Reflected
t	Target
TC	Thermocouple
x, y	Pixel location in array

CRediT authorship contribution statement

Manuela Sisti: Methodology, Experiments, Post-processing, Original draft preparation, Writing – review & editing. **Chiara Falsetti:** Supervision, Experiments, Original draft preparation, Writing – review & editing. **Paul F. Beard:** Supervision, Writing – review & editing.

Declaration of competing interest

The authors declare that they have no known competing financial interests or personal relationships that could have appeared to influence the work reported in this paper.

Data availability

Data will be made available on request.

References

[1] G. Carlomagno, G. Cardone, Infrared thermography for convective heat transfer measurements, Exp. Fluids 49 (2010) 1187–1218, http://dx.doi.org/10.1007/s00348-010-0912-2.

[2] C. Falsetti, M. Sisti, P. Beard, Infrared thermography and calibration techniques for gas turbine applications: a review, Infrared Phys. Technol. 113 (2021) 103574, http://dx.doi.org/10.1016/j.infrared.2020.103574.

[3] M. Martiny, R. Schiele, M. Gritsch, A. Schulz, S. Wittig, In situ calibration for quantitative infrared thermography, QIRT 96 - Eurotherm Series 50 Stuttgart, Germany (1996) http://dx.doi.org/10.21611/qirt.1996.001.

[4] A. Schulz, Infrared thermography as applied to film cooling of gas turbine components, Meas. Sci. Technol. 11 (2000) 948, http://dx.doi.org/10.1088/0957-0233/11/7/311.

[5] M. Ochs, T. Horbach, A. Schulz, R. Koch, H. Bauer, A novel calibration method for an infrared thermography system applied to heat transfer experiments, Meas. Sci. Technol. 20 (2009) 075103, http://dx.doi.org/10.1088/0957-0233/20/7/075103.

[6] M. Elfner, T. Glasenapp, A. Schulz, H.-J. Bauer, A spatially resolved in situ calibration applied to infrared thermography, Meas. Sci. Technol. 30 (8) (2019) 085201, http://dx.doi.org/10.1088/1361-6501/ab1db5.

[7] B. Kirollos, T. Povey, High-accuracy infrared thermography method using reflective marker arrays, Meas. Sci. Technol. 28 (2017) 095405, http://dx.doi.org/10.1088/1361-6501/aa7f0d.

[8] I. Jonsson, V. Chernoray, R. Dhanasegaran, Infrared thermography investigation of heat transfer on outlet guide vanes in a turbine rear structure, Int. J. Turbomach. Propuls. Power 5 (3) (2020) https://www.mdpi.com/2504-186X/5/3/23.

[9] M. Mori, L. Novak, M. Sekavcnik, Measurements on rotating blades using IR thermography, Exp. Therm Fluid Sci. 32 (2) (2007) 387–396, http://dx.doi.org/10.1016/j.expthermflusci.2007.05.002.

[10] S. Lazzi Gazzini, R. Schader, A.L. Kalfas, R.S. Abhari, Infrared thermography with non-uniform heat flux boundary conditions on the rotor endwall of an axial turbine, Meas. Sci. Technol. 28 (2) (2017) 025901, http://dx.doi.org/10.1088/1361-6501/aa5174.

[11] L. Christensen, R. Celestina, S. Sperling, R. Mathison, H. Aksoy, J. Liu, Infrared temperature measurements of the blade tip for a turbine operating at corrected engine conditions, Proc. ASME Turbo Expo 7 (2020).

[12] B. Knisely, R. Berdanier, K. Thole, C. Haldeman, J. Markham, J. Cosgrove, A. Carlson, J. Scire, Acquisition and processing considerations for infrared images of rotating turbine blades, ASME J. Turbomach. 143 (4) (2021) 041013, http://dx.doi.org/10.1115/1.4050143.

[13] B. Knisely, R. Berdanier, K. Thole, C. Haldeman, Effects of part-to-part flow variation on overlall effectiveness and life of rotating turbine blades, Proc. ASME Turbo Expo 2022 (2022) http://dx.doi.org/10.1115/GT2022-83216, Volume 6A: Heat Transfer – Combustors; Film Cooling, V06AT12A042.

[14] K.S. Chana, D.N. Cardwell, T.V. Jones, A review of the oxford turbine research facility, Proc. ASME Turbo Expo (2013) http://dx.doi.org/10.1115/GT2013-95687, Volume 3C: Heat Transfer, V03CT14A026.

[15] C. Falsetti, P. Beard, D. Cardwell, K. Chana, A review of high-speed rotating HP turbine heat transfer and cooling studies over the last decade in the oxford turbine research facility, Proc. ASME Turbo Expo 2022 10B (2022) http://dx.doi.org/10.1115/GT2022-81945.

[16] M. Sisti, C. Falsetti, K. Chana, P. Beard, Infrared temperature measurements on high pressure turbine blades in the oxford turbine research facility: calibration and image processing techniques, in: Proceedings of 14th European Conference on Turbomachinery Fluid dynamics & Thermodynamics, 2021, http://dx.doi.org/10.29008/ETC2021-780.

[17] CI Systems, SR-33N integrated compact extended area blackbody, 2023, URL https://www.ci-systems.com/Files/SR-33N_June_2021%20.pdf, last accessed 17 August 2023.
[18] Fluke, Fluke calibration 4180/4181 precision IR calibrators, 2023, URL https://www.fluke.com/en-gb/product/calibration-tools/temperature-calibrators/fluke-calibration-4180-4181/ds, Last accessed 17 August 2023.
[19] M. Schulz, L. Caldwell, Nonuniformity correction and correctability of infrared focal plane arrays, Infrared Phys. Technol. 36 (4) (1995) 763–777, http://dx.doi.org/10.1016/1350-4495(94)00002-3.
[20] S. Gao, L. Wang, C. Feng, K. Kipngetich, Analyzing the influence of combustion gas on a gas turbine by radiation thermometry, Infrared Phys. Technol. 79 (2015) 184–193.
[21] LabFacility, Temperature handbook, 2023, URL https://www.labfacility.com/pub/media/pdf/temperature-handbook-9-to-13.pdf, Last accessed 17 August 2023.
[22] J. Manara, M. Zips, T. Stark, M. Arduini, H.-P. Erbert, A. Tutschke, A. Hallam, J. Hanspal, M. Langley, D. Hodge, J. Hartmann, Long wavelength infrared radiation thermometry for non-contact temperature measurements in gas turbines, Infrared Phys. Technol. 80 (2017) 120–130, http://dx.doi.org/10.1016/j.infrared.2016.11.014.
[23] Crystran, Zinc selenide material properties, 2023, URL https://www.crystran.co.uk/optical-materials/zinc-selenide-znse, Last accessed 26 August 2023.
[24] H. Qi, X. Zhang, M. Jiang, C. Liu, Q. Wang, D. Li, Optical properties of zinc selenide slabs at 373 and 423 K in the wavelength 2–15 μm, Optik 127 (2016) 5576–5584, http://dx.doi.org/10.1016/j.ijleo.2016.03.079.